Electronic Supplementary Material (ESI) for Inorganic Chemistry Frontiers.

Supporting Information

Solid-State *versus* Solution Investigation of a Luminescent Chiral BINOL Derived Bisphosphate Single-Molecule Magnet

Carlo Andrea Mattei,[a] Vincent Montigaud,[a] Frédéric Gendron,[a] Sandrine Denis-Quanquin,[b] Vincent Dorcet,[a] Nicolas Giraud,[c] François Riobé,[b] Gilles Argouarch,[a] Olivier Maury,[b] Boris Le Guennic,*[a] Olivier Cador,[a] Claudia Lalli,[a] Fabrice Pointillart*[a]

[a] *Univ Rennes, CNRS, ISCR (Institut des Sciences Chimiques de Rennes) - UMR 6226, 35000 Rennes, France*

[b] *Laboratoire de Chimie de l'ENS-LYON-UMR 5182, 46 Allée d'Italie, 69364 Lyon Cedex 07, France*

[c] *Laboratory of Pharmacological and Toxicological Chemistry and Biochemistry Université Paris Descartes, Sorbonne Paris Cité, 45 rue des Saints Pères, 75006 Paris, France*

Corresponding author's email: boris.leguennic@univ-rennes1.fr; fabrice.pointillart@univ-rennes1.fr

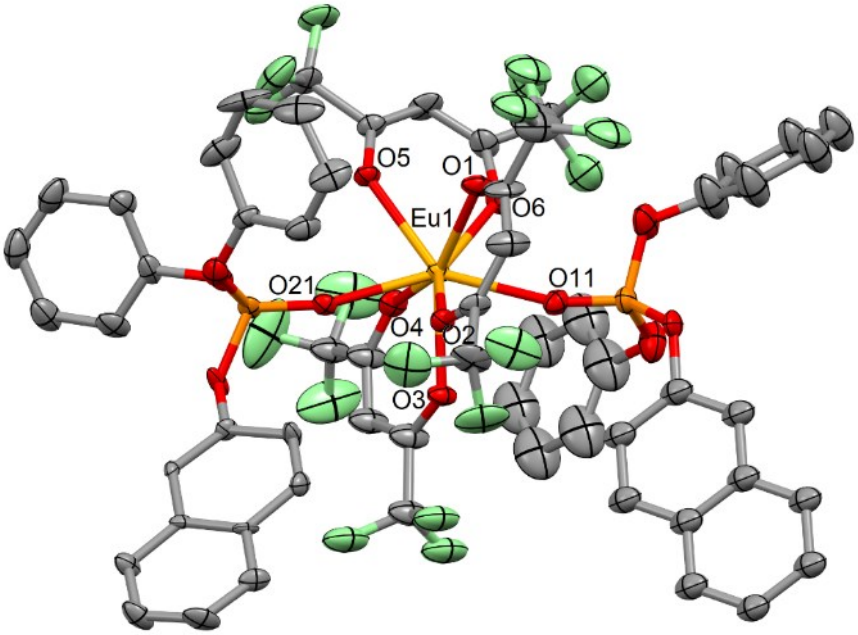

Figure S1. Ortep view of the molecular structure of **[(*S*)-2]$_n$**.

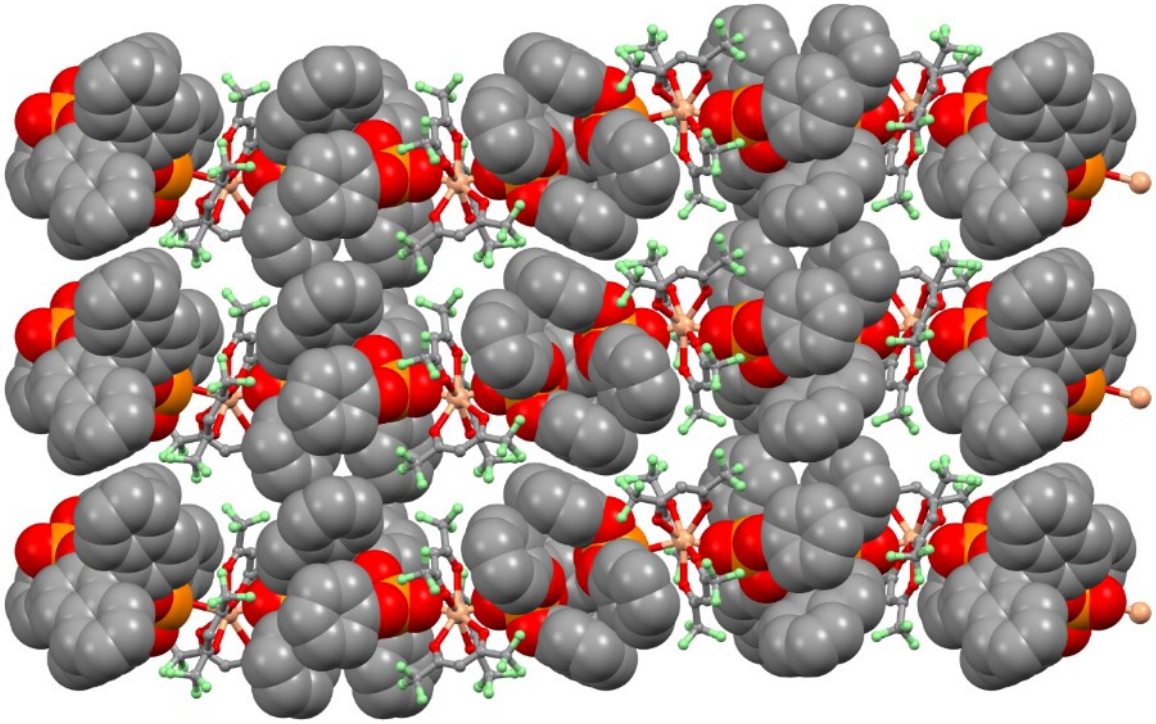

Figure S2. Crystal packing of **[(*S*)-2]$_n$** in the plane (101). **(*S*)-L** ligand and Eu(hfac)$_3$ units are respectively displayed in spacefill and ball and sticks representations.

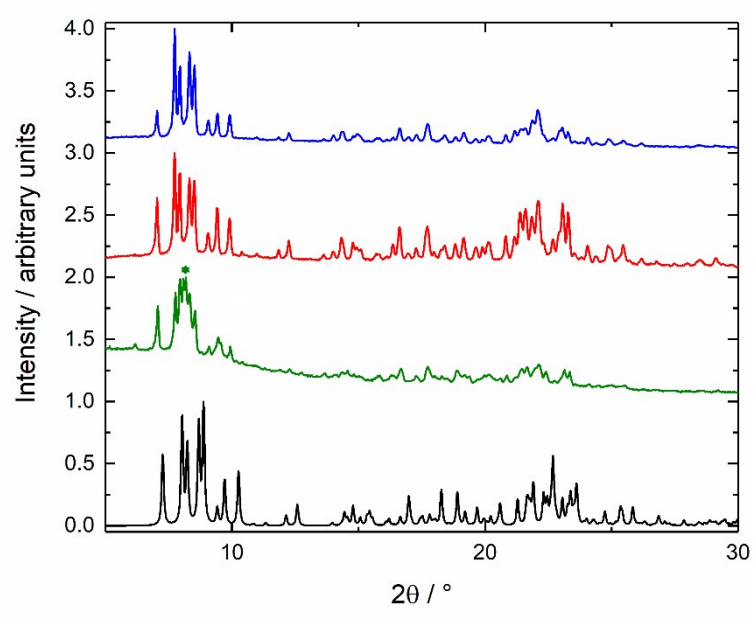

Figure S3. Superposition of experimental powder X-ray diffraction patterns from **[(*S*)-1]$_n$** (blue), **[(*S*)-2]$_n$** (red) and **[(*S*)-3]$_n$** (green) measured at 300 K and simulated from **[(*R*)-2]$_n$** single-crystal data obtained at 150 K (black). *unknown specie not observed by NMR.

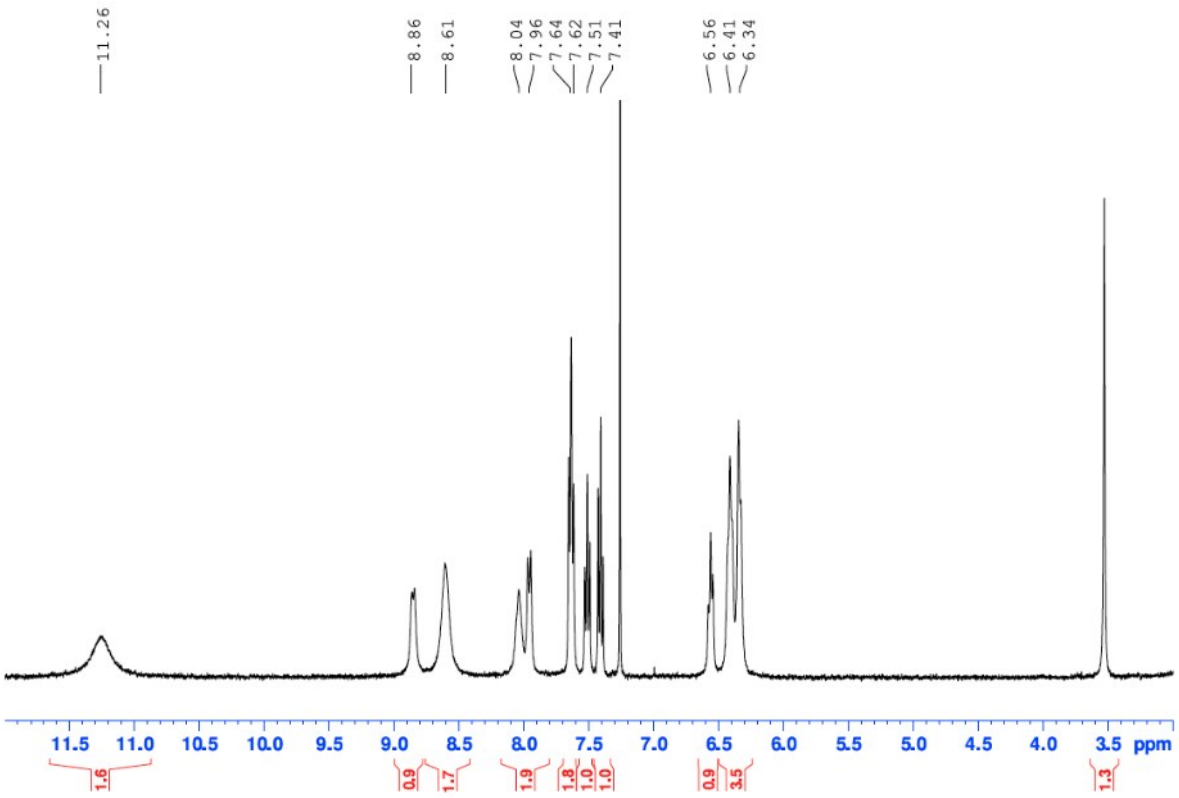

Figure S4. ^{1}H NMR (400 MHz) spectrum for **[(*S*)-2]** in $CDCl_3$ at room temperature.

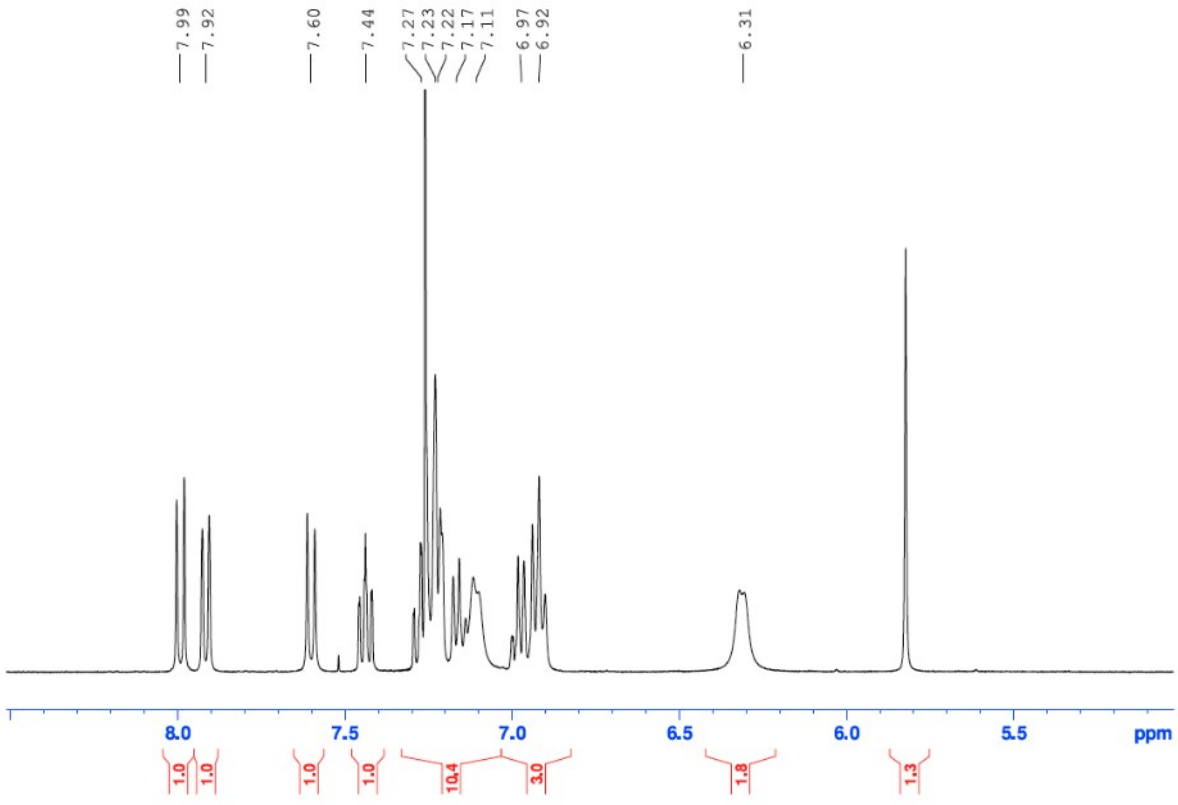

Figure S5. ^{1}H NMR (400 MHz) spectrum for **[(*S*)-3]** in $CDCl_3$ at room temperature.

NMR diffusion method

NMR diffusion experiments use a pair of gradients along the Z axis for spatial encoding of the signals. The 1st pulse field gradient (PFG) dephases the signal and the 2nd PFG refocuses it. Both gradients are separated by a delay (diffusion time) during which molecules diffuse: if the molecule moves along Z during the diffusion time, the signal is not fully refocused and so is decreased. The further the molecule goes, the more the signal is decreased. Spectra with increasing gradient strength are acquired and the intensity of each signal is a function of the gradient strength and the diffusion coefficient:

$$I = I_0 exp\left[-\gamma^2 \delta^2 G^2 \left(\Delta - \frac{\delta}{3} \right) D \right] \qquad \text{(S1)}$$

where I_0 is the intensity without gradient, γ is the gyromagnetic ratio of the observed nucleus, δ is the duration of the gradient pulse, G is the gradient strength and Δ is the diffusion time. The diffusion coefficient was determined for each ^{1}H resonances for **[(*S/R*)-2]** or **[(*S/R*)-3]** and the experimental data were fitted to Eq(S1). The global D_{obs} coefficient for the desired complex was obtained by averaging the diffusion coefficients of each proton (Table S4).

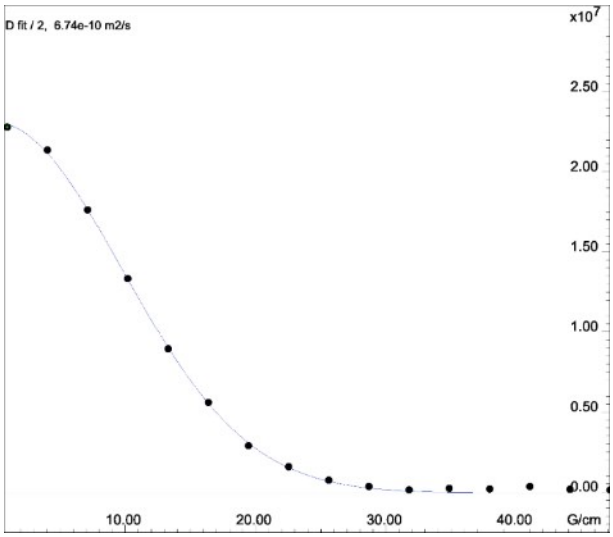

Figure S6. ^{1}H decaying curves recorded for one of the signals from **[(*S*)-2]** by varying the gradient strength in a standard PGSE experiment. The fit of the experimental data to the model curve corresponding to eq. (S1) gives a diffusion coefficient D = 674 $\mu m^2.s^{-1}$.

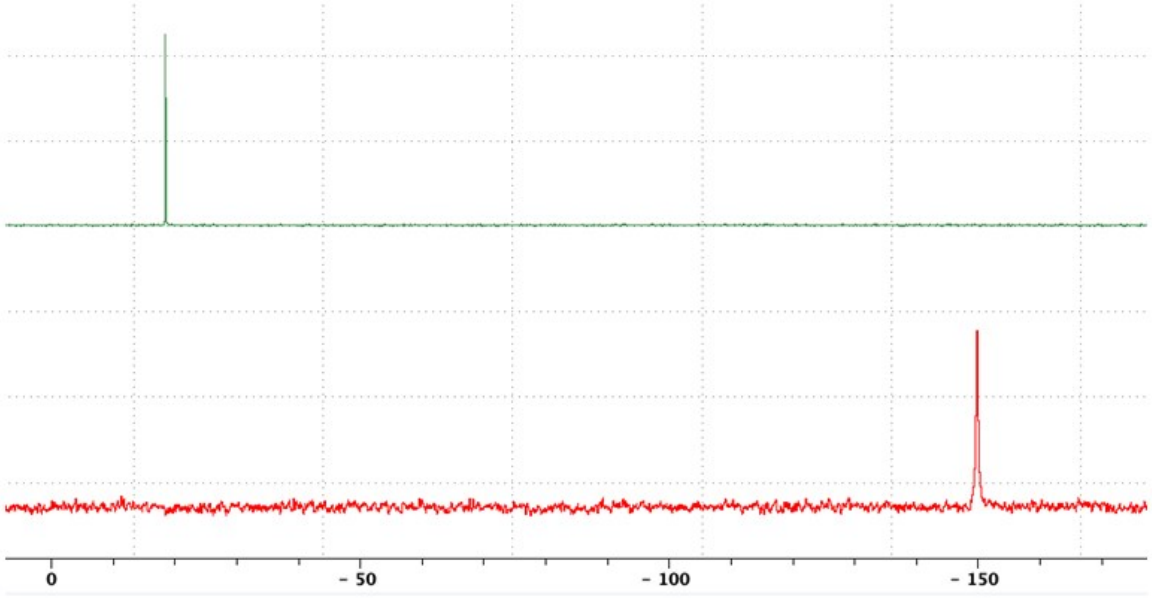

Figure S7. ^{31}P NMR (121.5 MHz) spectrum for **(*S*)-L** (green) and **[(*S*)-2]** in $CDCl_3$ at room temperature.

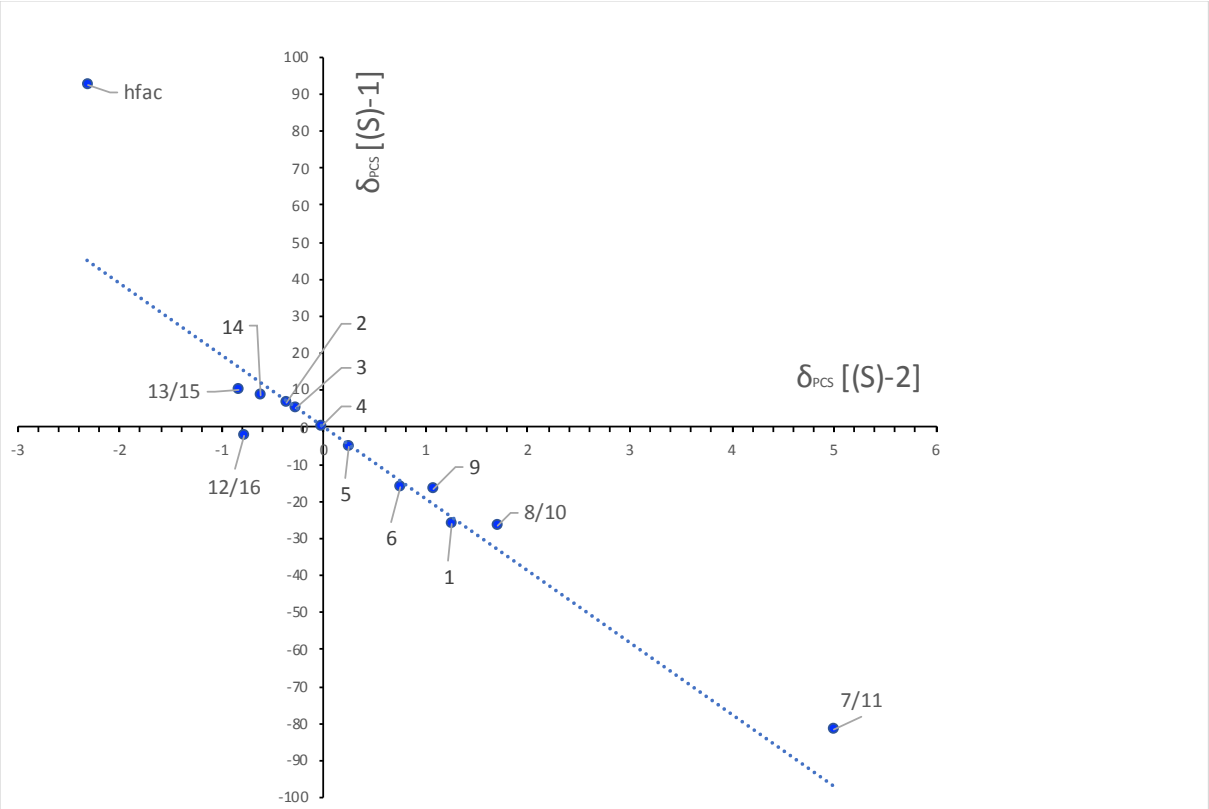

Figure S8. Plot of the pseudo-contact shifts determined in **[(*S*)-1]** against those in **[(*S*)-2].**

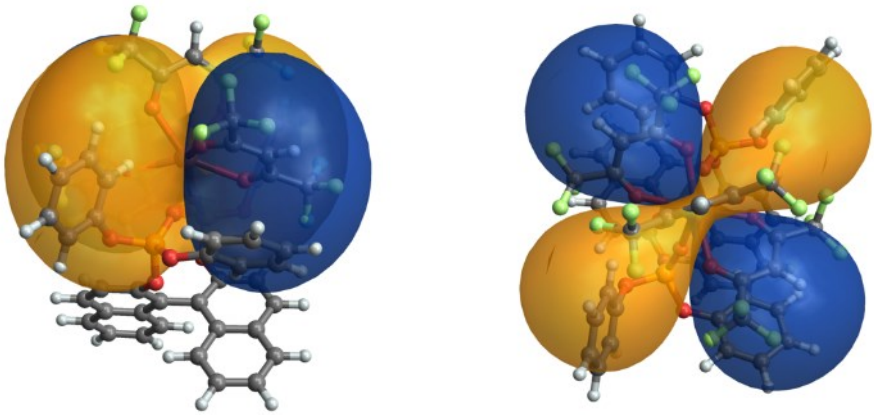

Figure S9. Isosurface depicting the pseudo-contact shift (PCS) induced by Dy(III) plotted on the structure of **[(*S*)-1]**. Blue and orange surfaces identify the spatial locations of positive and negative PCSs, respectively, by ± 20 ppm. The PCS isosurfaces constitute a representation of the anisotropy component of the magnetic susceptibility tensor χ of the metal ion.

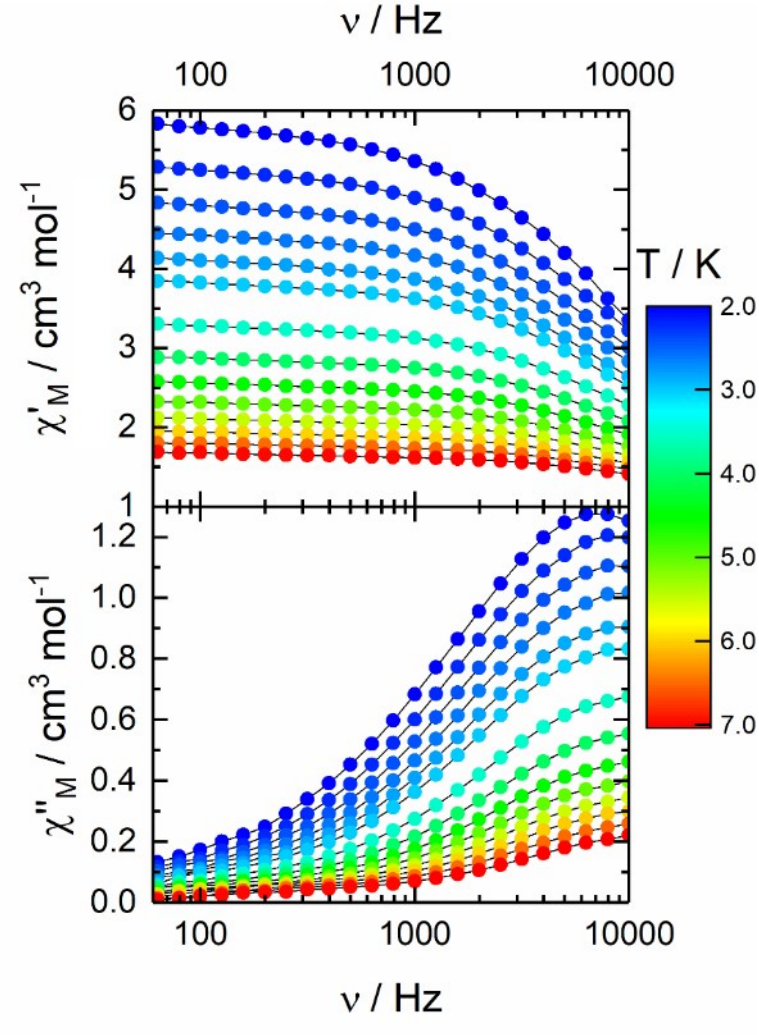

Figure S10. Frequency dependence of χ_M' and χ_M'' between 2 and 7 K for **[(*S*)-1]$_n$** at 0 Oe.

Extended Debye model used for [(*S*)-1]$_n$ in zero applied magnetic field:

$$\chi_M' = \chi_S + (\chi_T - \chi_S)\frac{1+(\omega\tau)^{1-\alpha}\sin\left(\alpha\frac{\pi}{2}\right)}{1+2(\omega\tau)^{1-\alpha}\sin\left(\alpha\frac{\pi}{2}\right)+(\omega\tau)^{2-2\alpha}}$$

$$\chi_M'' = (\chi_T - \chi_S)\frac{(\omega\tau)^{1-\alpha}\cos\left(\alpha\frac{\pi}{2}\right)}{1+2(\omega\tau)^{1-\alpha}\sin\left(\alpha\frac{\pi}{2}\right)+(\omega\tau)^{2-2\alpha}}$$

With χ_T the isothermal susceptibility, χ_S the adiabatic susceptibility, τ the relaxation time and α an empiric parameter which describe the distribution of the relaxation time. For SMM with only one relaxing object α is close to zero. The extended Debye model was applied to fit simultaneously the experimental variations of χ_M' and χ_M'' with the frequency ν of the oscillating field ($\omega = 2\pi\nu$). Typically, only the temperatures for which a maximum on the χ_M'' vs. ν curves, have been considered (see figure here below for an example). The best fitted parameters τ, α, χ_T, χ_S are listed in Table S8 with the coefficient of determination R^2.

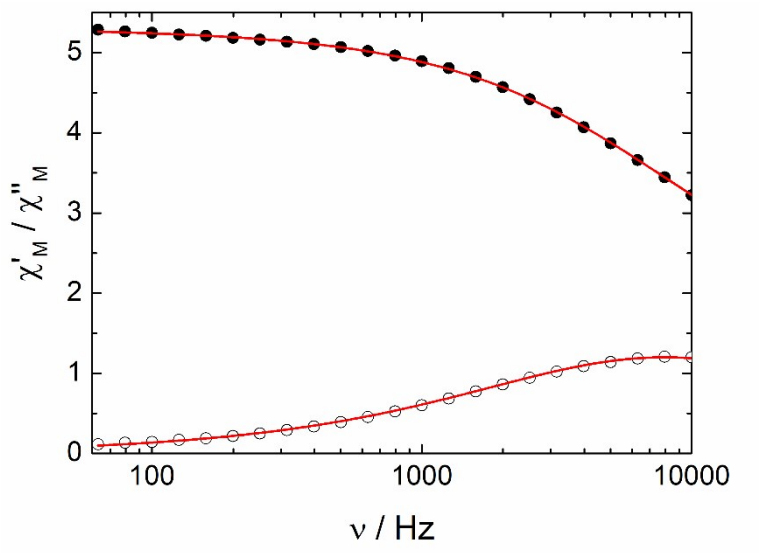

Figure S11. Frequency dependence of the in-phase (χ_M') (full black circles) and out-of-phase (χ_M'') (open circles) components of the ac susceptibility measured on powder at 2.2 K and 0 Oe with the best fitted curves (red lines) for **[(*S*)-1]$_n$**.

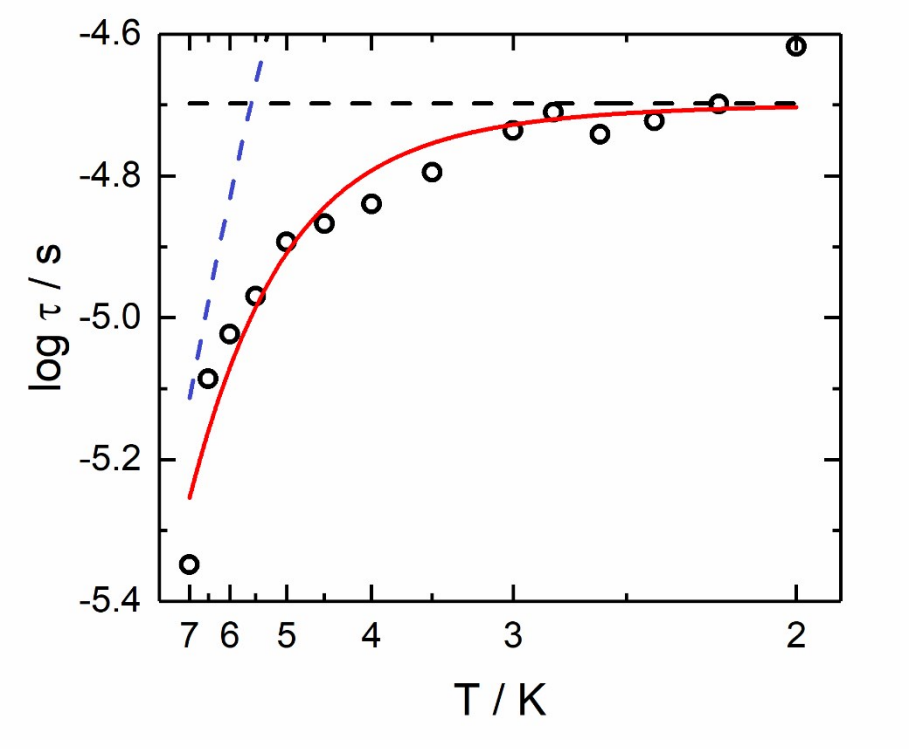

Figure S12. Temperature dependences of the relaxation times (τ) at 0 Oe in the temperature range 2-7 K (open circles) for **[(*S*)-1]$_n$**. Red lines are the best fitted curves while blue and black dashed lines represent respectively the Raman and QTM contributions with parameters given in the text.

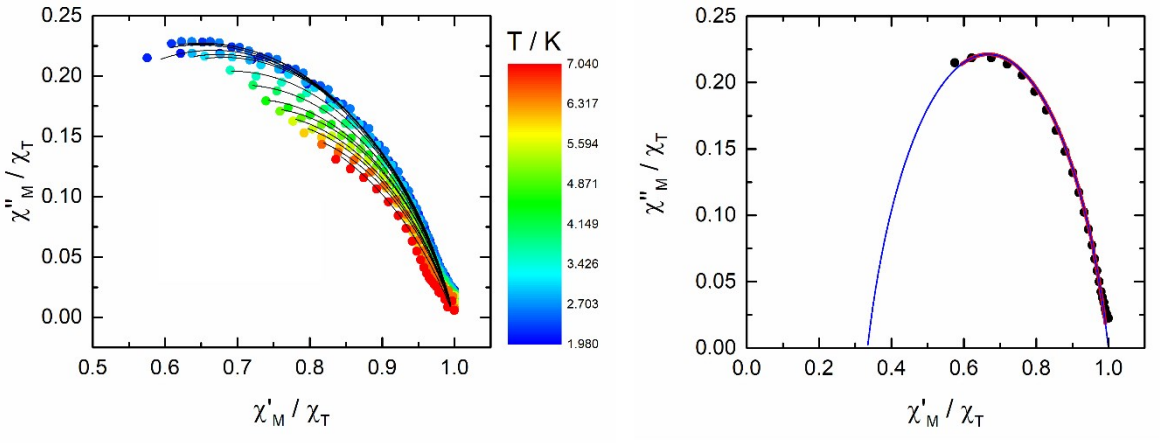

Figure S13. Normalized Cole-Cole plot at several temperatures between 2 and 7 K (left) and with extrapolation at 2 K (right) for **[(*S*)-1]$_n$**.

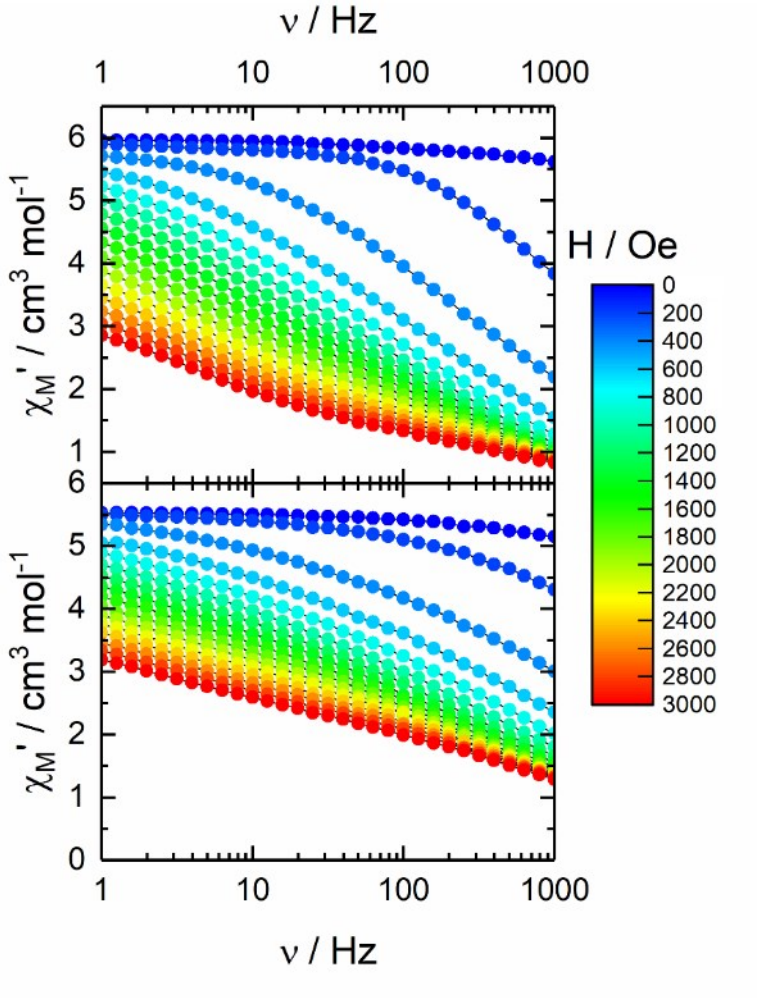

Figure S14. Frequency dependence of χ_M' at 2 K at various external fields for **[(*S*)-1]$_n$** (top) and **[(*S*)-1]** (frozen CH_2Cl_2 solution C=3×10^{-2} mol L^{-1}, down).

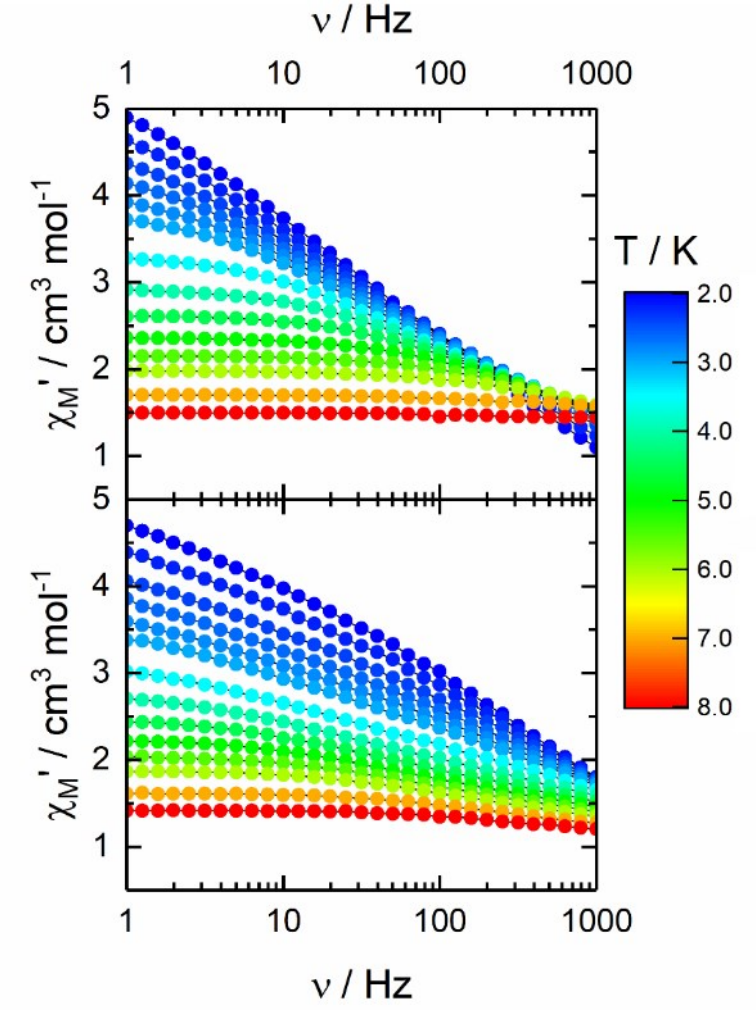

Figure S15. Frequency dependence of χ_M' between 2 and 8 K for **[(*S*)-1]$_n$** (top) and **[(*S*)-1]** (frozen CH_2Cl_2 solution C=3×10^{-2} mol L^{-1}, down) under an applied magnetic field of 1000 Oe.

Extended Debye model used for $[(S)\text{-}1]_n$ and $[(S)\text{-}1]$ in applied field.

$$\chi_M' = \chi_S + (\chi_T - \chi_S)\left\{\frac{\beta\left[1 + (\omega\tau_1)^{1-\alpha_1}\sin\left(\frac{\pi}{2}\alpha_1\right)\right]}{1 + 2(\omega\tau_1)^{1-\alpha_1}\sin\left(\frac{\pi}{2}\alpha_1\right) + (\omega\tau_1)^{2(1-\alpha_1)}} + \frac{(1-\beta)\left[1 + (\omega\tau_2)^{1-\alpha_2}\sin\left(\frac{\pi}{2}\alpha_2\right)\right]}{1 + 2(\omega\tau_2)^{1-\alpha_2}\sin\left(\frac{\pi}{2}\alpha_2\right) + (\omega\tau_2)^{2(1-\alpha_2)}}\right\}$$

$$\chi_M'' = (\chi_T - \chi_S)\left\{\frac{\beta\left[(\omega\tau_1)^{1-\alpha_1}\cos\left(\frac{\pi}{2}\alpha_1\right)\right]}{1 + 2(\omega\tau_1)^{1-\alpha_1}\sin\left(\frac{\pi}{2}\alpha_1\right) + (\omega\tau_1)^{2(1-\alpha_1)}} + \frac{(1-\beta)\left[(\omega\tau_2)^{1-\alpha_2}\cos\left(\frac{\pi}{2}\alpha_2\right)\right]}{1 + 2(\omega\tau_2)^{1-\alpha_2}\sin\left(\frac{\pi}{2}\alpha_2\right) + (\omega\tau_2)^{2(1-\alpha_2)}}\right\}$$

With χ_T the isothermal susceptibility, χ_S the adiabatic susceptibility, τ the relaxation time and α an empiric parameter which describe the distribution of the relaxation time. For SMM with only one relaxing object α is close to zero. The extended Debye model was applied to fit simultaneously the experimental variations of χ_M' and χ_M'' with the frequency ν of the oscillating field ($\omega = 2\pi\nu$). The best fitted parameters τ_1, α_1, χ_{1T}, χ_{1S}, τ_2, α_2, χ_{2T} and χ_{2S} are listed in Tables S10 and S11 with the coefficient of determination R^2. τ_1, α_1, χ_{1T}, χ_{1S} are parameters for the high frequency contribution while τ_2, α_2, χ_{2T} and χ_{2S} are for the low frequency contribution.

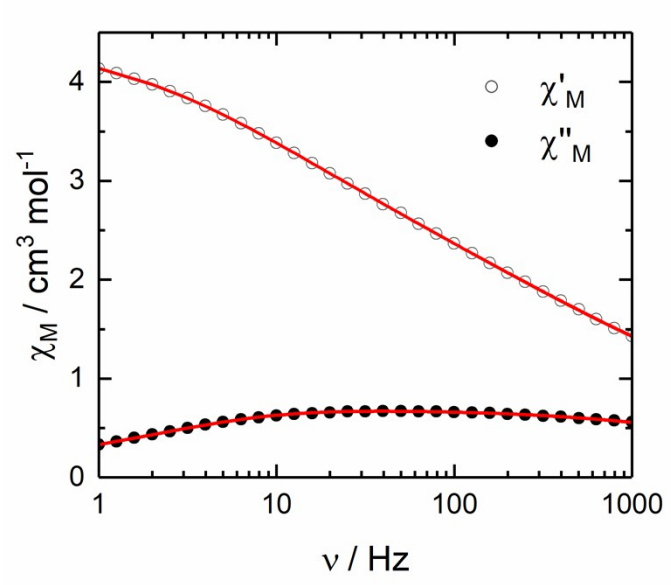

Figure S16. Frequency dependence of the in-phase (χ_M') and out-of-phase (χ_M") components of the ac susceptibility measured on powder at 2.6 K and 1000 Oe with the best fitted curves (red lines) for **[(*S*)-1]$_n$**.

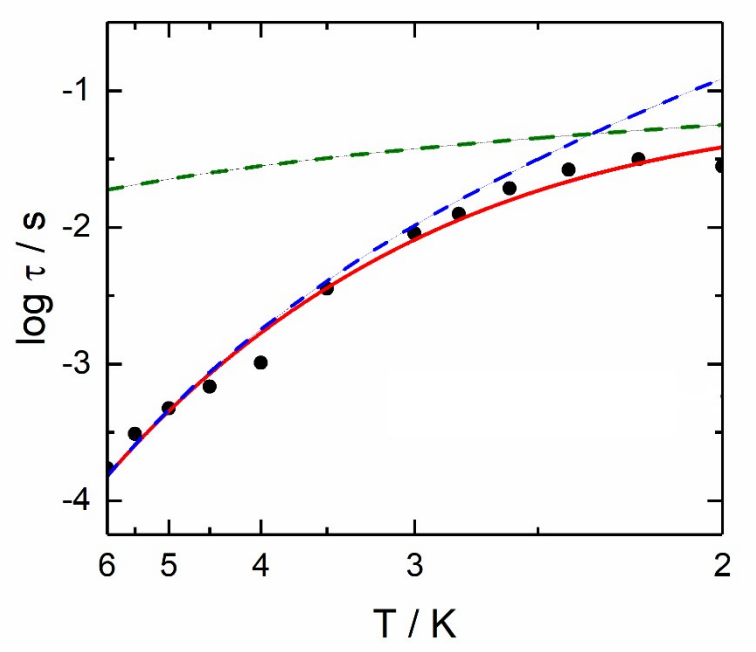

Figure S17. Thermal variation of the relaxation time of **[(*S*)-1]$_n$** for the LF contribution (black dots) with the best fitted curve in red and the separated Direct process (dashed green line) and Raman process (dashed blue line).

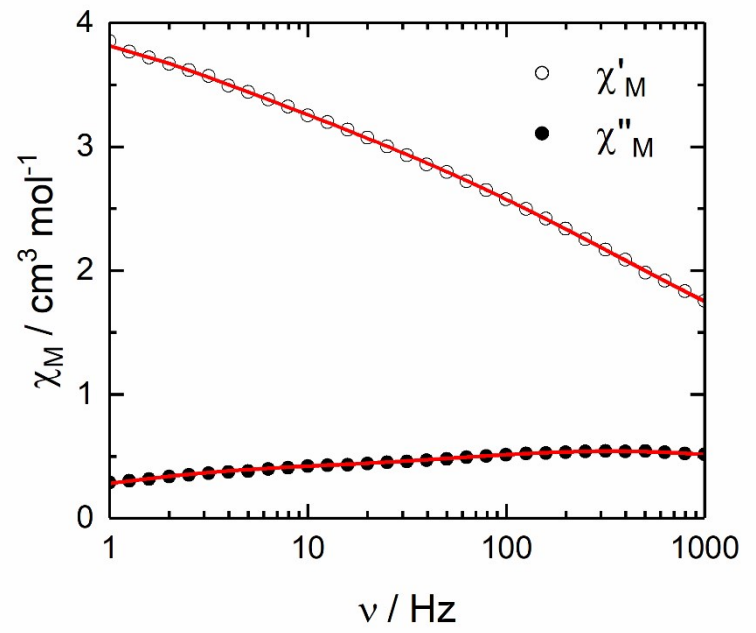

Figure S18. Frequency dependence of the in-phase (χ_M') and out-of-phase (χ_M") components of the ac susceptibility measured on powder at 2.6 K and 1000 Oe with the best fitted curves (red lines) for **[(*S*)-1]**.

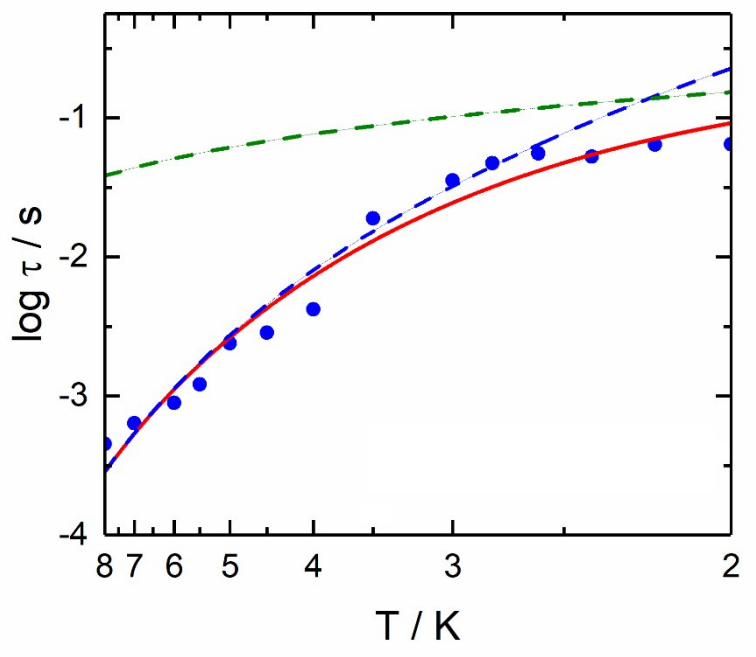

Figure S19. Thermal variation of the relaxation time of **[(*S*)-1]** for the LF contribution (blue dots) with the best fitted curve in red and the separated Direct process (dashed green line) and Raman process (dashed blue line).

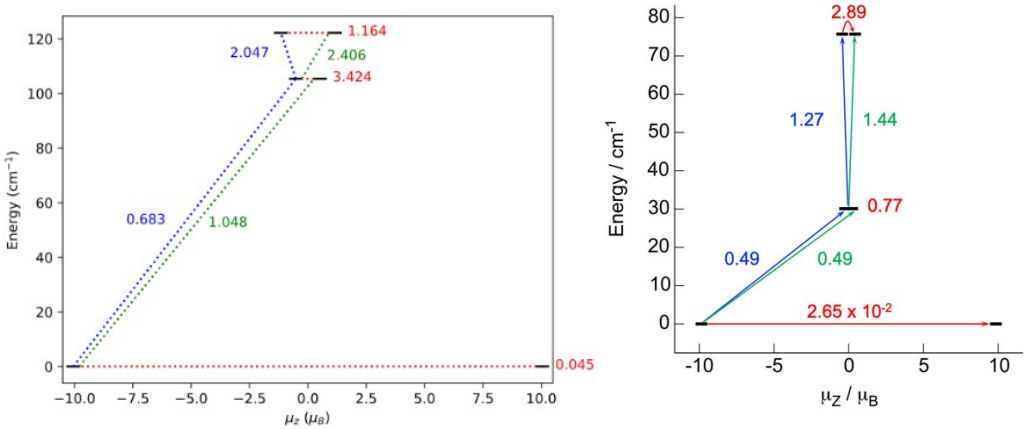

Figure S20. Energies (in cm^{-1}) and μ_z (in μ_B) values for the three lowest Kramers doublet states of the solution (left) and solid-state (right) species. The values of the magnetic (i.e. isotropic Zeeman) transition moments between the states are given for comparison. The values in horizontal correspond to QTM (for the GS) and TA-QTM (for the ESs) mechanisms of the magnetization relaxation, whereas vertical and diagonal values correspond to Orbach mechanisms.

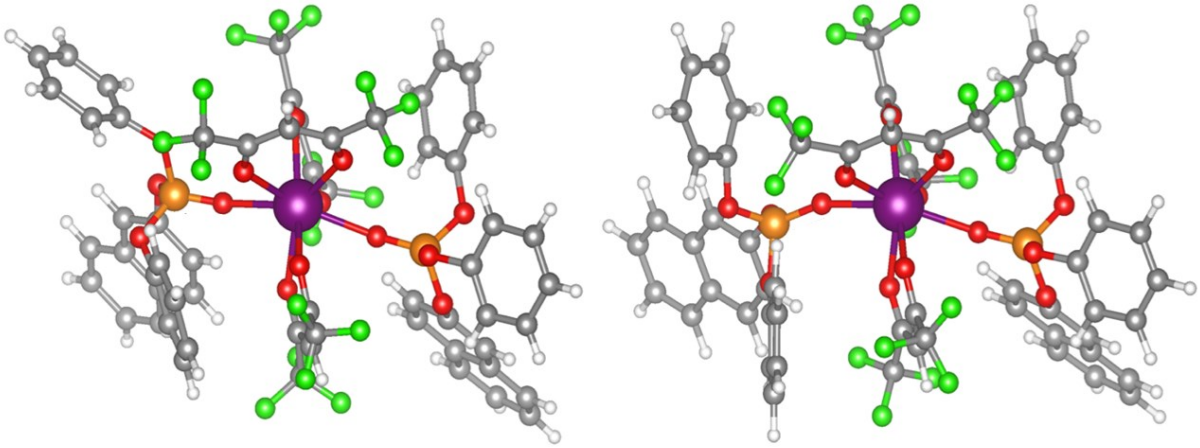

Figure S21. Representation of the **[(*S*)-1]$_n$** corresponding to 74 % occupancy position (left) and **[(*S*)-1]$_n$'** corresponding to 26 % occupancy position (right) models corresponding the two possible configurations of the left-hand side phosphate ligand.

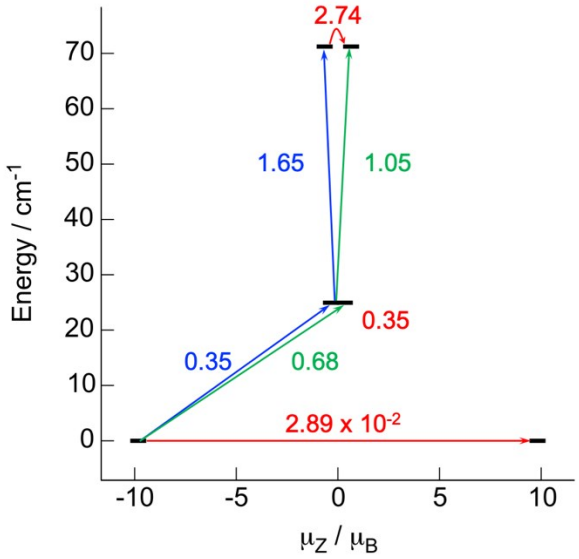

Figure S22. Energies (in cm^{-1}) and μ_z (in μ_B) values for the three lowest Kramers doublet states of **[(*S*)-1]$_n$'**. The values of the magnetic (i.e. isotropic Zeeman) transition moments between the states are given for comparison. The values in horizontal correspond to QTM (for the GS) and TA-QTM (for the ESs) mechanisms of the magnetization relaxation, whereas vertical and diagonal values correspond to Orbach mechanisms.

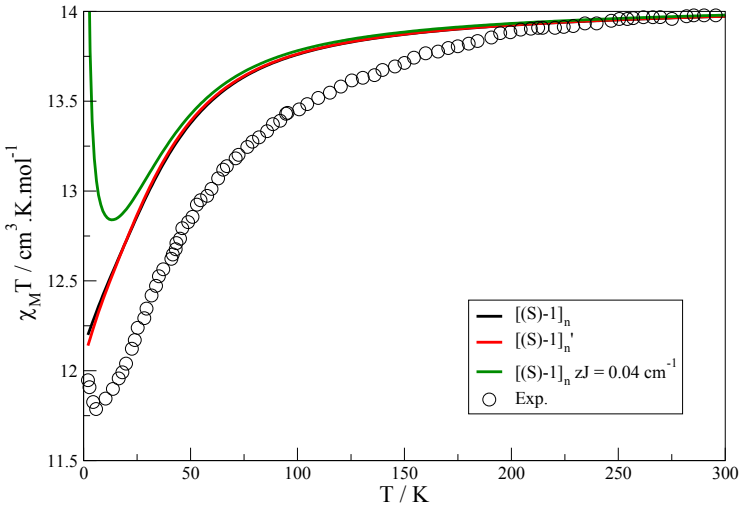

Figure S23. Thermal dependence of $\chi_M T$ for **[(*S*)-1]$_n$** (solid-state measurements) (black circles). Black and red lines correspond the ab initio computational results obtained respectively with the solid-state **[(*S*)-1]$_n$** and **[(*S*)-1]'$_n$** model compounds (see text for details) while green line corresponds to the calculations taking into account dipolar interactions (zJ' = 0.04 cm^{-1}).

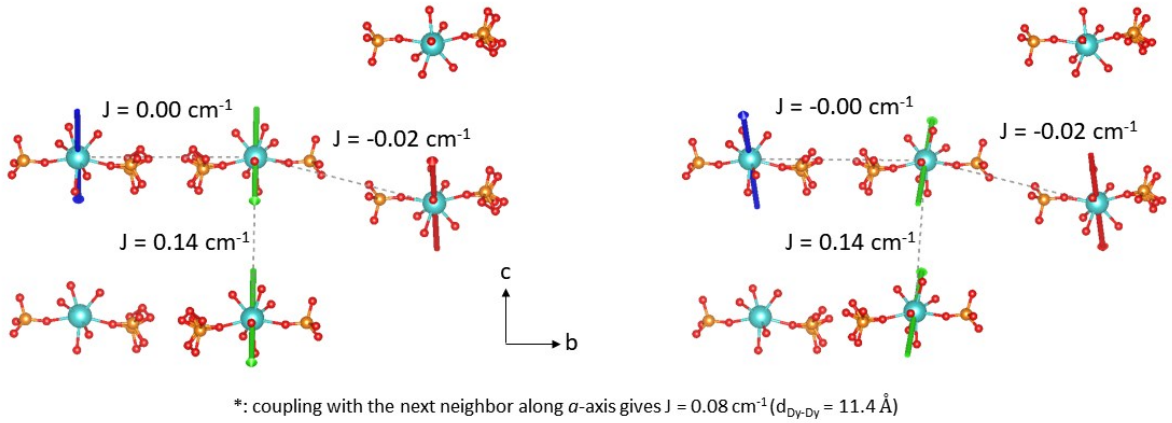

Figure S24. Representation of the dipolar interactions considered for **[(*S*)-1]$_n$** (left) and **[(*S*)-1]'$_n$** (right).

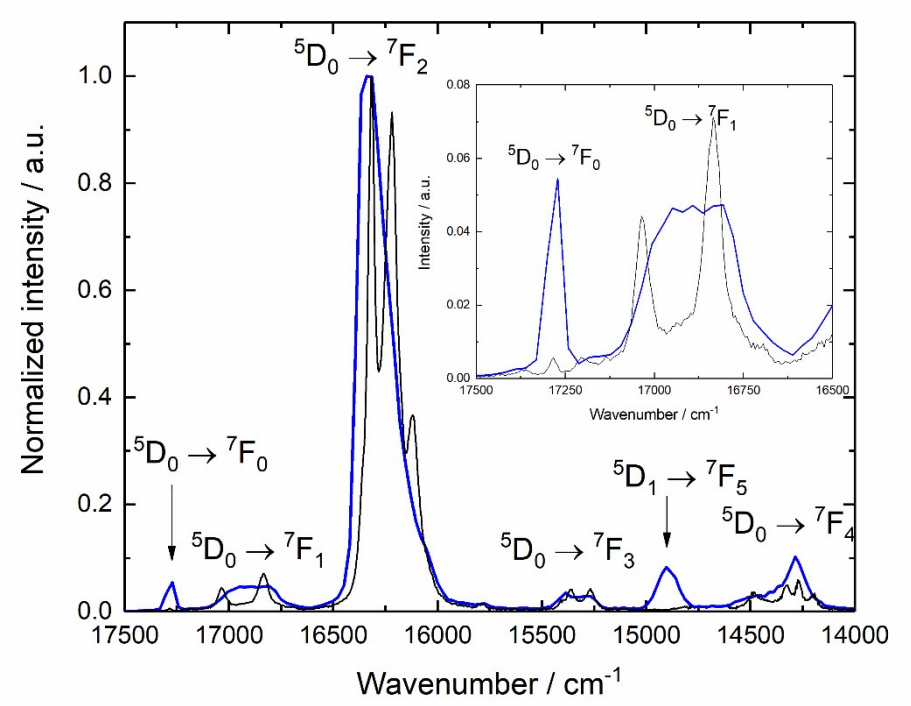

Figure S25. Emission spectra at room temperature under an irradiation of 28570 cm^{-1} for **[(*S*)-2]** (blue line) and **[(*S*)-2]$_n$** (black line).

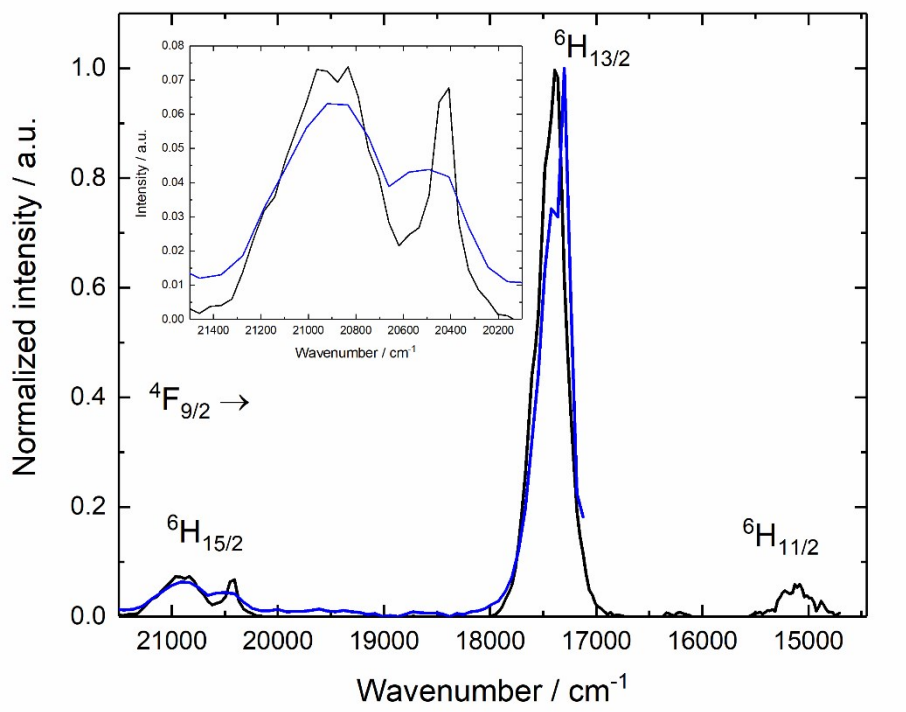

Figure S26. Emission spectra at room temperature under an irradiation of 28570 cm^{-1} for **[(*S*)-1]$_n$** (black line) and **[(*S*)-1]** (blue line).

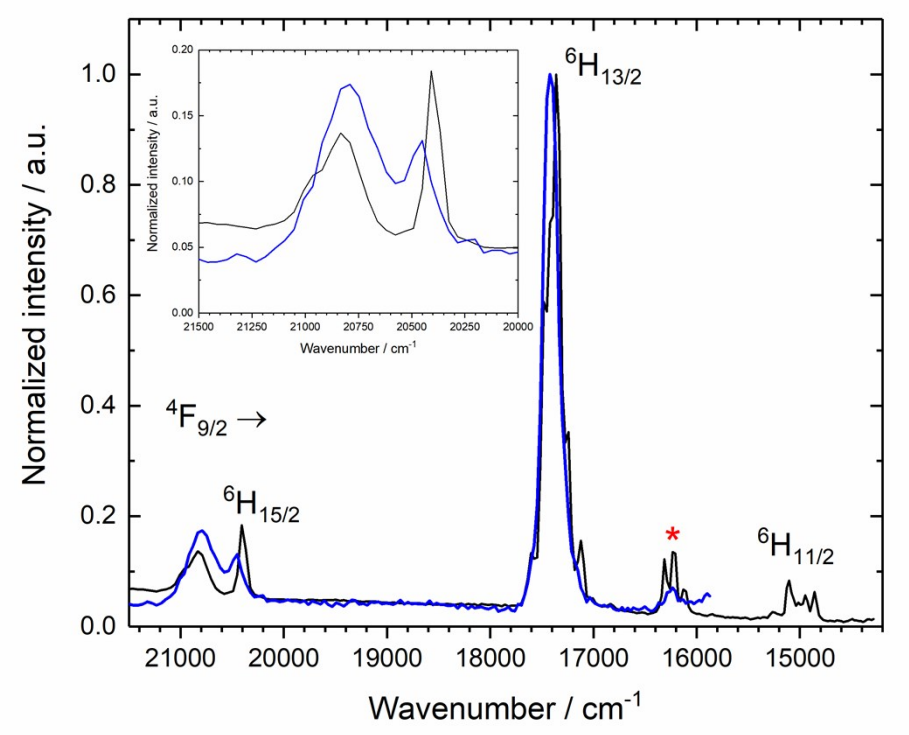

Figure S27. Emission spectra at 77 K under an irradiation of 28570 cm^{-1} for **[(*S*)-1]$_n$** (black line) and **[(*S*)-1]** (blue line).

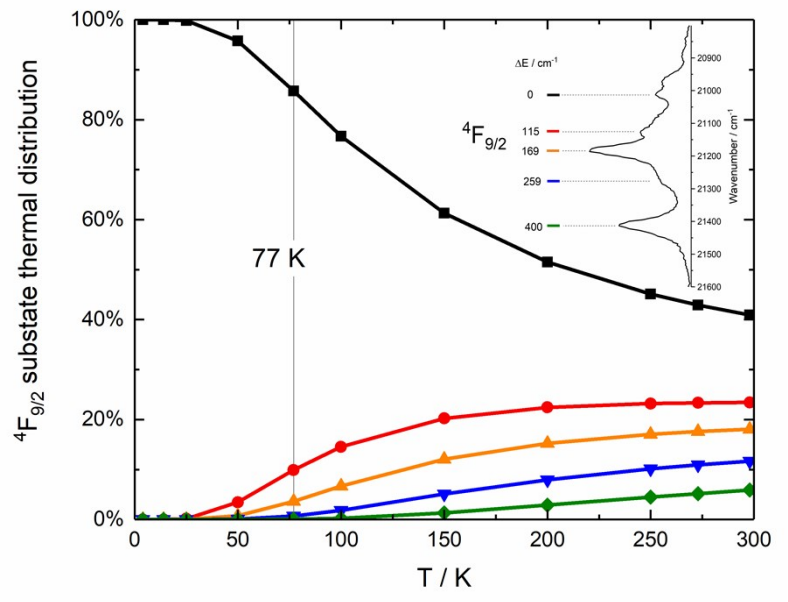

Figure S28. Boltzmann population of the M_J sub-levels of the $^4F^{9/2}$ excited state for **[(*S*)-1]$_n$**. (Inset) energy diagram of the $^4F_{9/2}$ excited state obtained from the solid-state excitation spectrum measured at 77 K.

Table S1. X-ray crystallographic data for **[(*R*)-2]$_n$**.

Compound	[Eu(hfac)$_3$((***R***)-**L**)]$_n$ **[(*R*)-2]$_n$**
Formula M / g.mol^{-1}	$C_{59}H_{35}EuyF_{18}O_{14}P_2$ 1523.8
Crystal system	Orthorhombic
Space group	$C222_1$ (N°20)
Cell parameters	a = 11.4660(8) Å b = 21.9976(14) Å c = 48.630(3) Å
Volume / Å^3	12265.7(14)
Z	8
T / K	150(2)
2θ range /°	$4.09 \leq 2\theta \leq 55.00$
ρ_{calc} / g.cm^{-3}	1.650
μ / mm^{-1}	1.194
Number of reflections	38999
Independent reflections	13684
R_{int}	0.0379
$Fo^2 > 2\sigma(Fo)^2$	12118
Number of variables	720
R_1, ωR_2	0.0754, 0.1633

Table S2. SHAPE analysis of the coordination polyhedra around the lanthanide in **[(*R*)-2]$_n$** and in the DFT optimized solution structure **[(*S*)-1]**.

Metal	$CShM_{SAPR-8}$ (square antiprism D_{4d})	$CShM_{BTPR-8}$ (biaugmented trigonal prism C_{2v})	$CShM_{TDD-8}$ (triangular dodecahedron D_{2d})
Eu1	0.330	1.788	2.138
Dy1	0.237	2.067	2.292

Table S3. Proton numbering. ^{1}H NMR relaxation times (T_1 given in ms) for **(*S*)-L**, and related **[(S)-1,2,3]** complexes in $CDCl_3$ at room temperature. Due to signals overlaps, some T_1 values were not determined and are marked with a *.

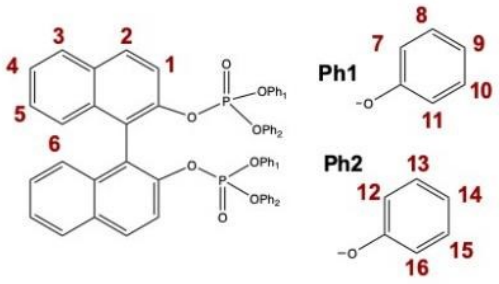

Proton	(*S*)-L	[(*S*)-3]	[(*S*)-2]	[(*S*)-1]
1	2200	1390	225	3
2	1350	1020	603	9
3	1390	1030	875	33
4	1450	1100	1072	80
5	1500	1340	1050	72
6	1840	*	1000	23
7/11	3400	1950	140	<1
8/10	3100	1800	748	10
9	3100	1800	1280	24
12/16	3500	*	313	<1
13/15	3000	*	858	15
14	3500	*	1580	32
hfac	no	1860	221	<1

Table S4. Diffusion coefficients determined for every proton from **[(*S*)-2]** and the calculated error.

Proton	δ **[ppm]**	**D [m^2.s^{-1}]**	**error**
1	8.87	6.66E-10	3.84E-12
2	7.66	6.75E-10	1.61E-12
3	7.68	6.63E-10	2.19E-12
4	7.43	6.90E-10	2.64E-12
5	7.54	6.85E-10	2.82E-12
6	7.97	6.77E-10	2.48E-12
7/11	11.28	6.61E-10	1.96E-11
8/10	8.63	6.70E-10	3.28E-12
9	8.06	6.70E-10	3.39E-12
12/16	6.37	6.79E-10	1.16E-12
13/15	6.44	6.71E-10	1.49E-12
14	6.59	6.68E-10	3.77E-12
hfac	3.55	6.74E-10	1.75E-12
CDCl3	7.28	2.37E-09	5.00E-11

Table S5. Experimental ^{1}H NMR chemical shifts (δ^{exp} in ppm) for **(*S*)-L** and related **[(*S*)-1,2,3]** complexes in $CDCl_3$ at room temperature (based on the analysis of 2D COSY and ^{13}C-HSQC, spectra not shown). Determined δ^{PCS} contribution for **[(*S*)-1,2]** using the following relationship:

Eq(3) δ^{exp} (**[(*S*)-1,2]**) = δ^{dia} (**[(*S*)-3]**) + δ^{PCS} (**[(*S*)-1,2]**)

Proton	(*S*)-L	[(*S*)-3]	[(*S*)-2]	[(*S*)-1]	δ^{PCS}([(*S*)-2])	δ^{PCS}([(*S*)-1])
1	7.78	7.6	8.86	-18.7	1.26	-26.3
2	7.93	7.99	7.62	14.77	-0.37	6.78
3	7.87	7.92	7.64	13.03	-0.28	5.11
4	7.41	7.44	7.41	7.82	-0.03	0.38
5	7.22	7.27	7.52	2.05	0.25	-5.22
6	7.17	7.22	7.97	-8.68	0.75	-15.9
7/11	6.56	6.31	11.3	-75.1	4.99	-81.41
8/10	7	6.92	8.63	-19.42	1.71	-26.34
9	6.99	6.97	8.05	-9.62	1.08	-16.59
12/16	6.88	7.11	6.33	4.78	-0.78	-3.11
13/15	7.14	7.23	6.4	17.27	-0.83	10.04
14	7.08	7.16	6.55	15.95	-0.61	8.79
hfac	no	5.82	3.5	98.2	-2.32	92.38

Table S6. Calculated ^{1}H chemical shifts (in ppm) using the Yttrium-based DFT optimized solution complex. The results are compared to the experimental values.

Proton	Calc.	δ [ppm]
1	8.5	7.6
2	8.6	7.99
3	7.9	7.92
4	7.7	7.44
5	7.7	7.27
6	8.4	7.22
7/11	5.5	6.31
8/10	7.1	6.92
9	7.2	6.97
12/16	7.9	7.11
13/15	7.7	7.23
14	7.5	7.16
hfac	5.8	5.82

Table S7. Calculated ^{1}H pseudo-contact shifts (PCSs - in ppm) for the solution complex. The results are compared to the experimental values.

Proton	Calc.	Calc. Averaged	δ^{PCS}(**[(*S/R*)-1]**)
1	-21.9 / -54.7	-38.3	-26.3
2	-19.6 / 20.9	0.6	6.78
3	-5.6 / 25.8	10.1	5.11
4	-2.4 / 19.6	8.6	0.38
5	-3.7 / 14.8	5.5	-5.25
6	-3.3 / 13.2	4.9	-15.9
7/11	-46.9 / -429.4	-238.1	-81.41
8/10	-31.1 / -114.9	-73.0	-26.34
9	-41.3	-41.3	-16.59
12/16	-3.8 / 15.5	5.85	-2.33
13/15	15.0 / 35.1	25.0	10.04
14	31.2	31.2	8.79
hfac	15.0 / 124.6 / 188.4	109.3	92.38

Table S8. Best fitted parameters (χ_T, χ_S, τ and α) with the extended Debye model for compound **[(*S*)-1]$_n$** at 0 Oe in the temperature range 2-7 K.

T	χs / cm^3 mol^{-1}	χ_T / cm^3 mol^{-1}	τ / s	α	R^2
2	1,94792	5,83694	2,41E-05	0,25339	0,99986
2.2	1,57801	5,30967	2,00E-05	0,27278	0,99998
2.4	1,45822	4,85318	1,89E-05	0,26626	0,99998
2.6	1,38158	4,46901	1,81E-05	0,26066	0,99997
2.8	1,44902	4,13399	1,95E-05	0,24745	0,99995
3	1,38915	3,84827	1,84E-05	0,24459	0,99996
3.5	1,27173	3,29879	1,60E-05	0,25393	0,99995
4	1,18693	2,88805	1,45E-05	0,26297	0,99995
4.5	1,1279	2,57171	1,36E-05	0,27167	0,99994
5	1,07273	2,3191	1,28E-05	0,26982	0,99995
5.5	0,96485	2,11733	1,07E-05	0,29316	0,99993
6	0,90416	1,94685	9,48E-06	0,30202	0,99994
6.5	0,86826	1,80168	8,20E-06	0,31273	0,99995
7	0,67586	1,68212	4,49E-06	0,36533	0,99994

Table S9. Best fitted parameters (χ_T, χ_S, τ and α) with the extended Debye model for compound **[(*S*)-1]$_n$** at 1000 Oe in the temperature range 2-6 K.

T / K	**$\chi_{T,1}$ / cm^3 mol^{-1}**	**χ_S / cm^3 mol^{-1}**	**τ_1 / s**	**α_1**	**$\chi_{t,2}$ / cm^3 mol^{-1}**	**α_2**	**τ_2 / s**	**R^2**
2	2.54161	0.11796	4.75E-04	0.44147	3.46505	0.52114	0.02804	2.43E-05
2.2	2.95992	0.11096	4.34E-04	0.49709	2.54416	0.47879	0.03152	8.85E-05
2.4	3.27784	0.11293	4.32E-04	0.55285	1.70828	0.41173	0.02636	3.41E-05
2.6	3.53466	0.14515	5.17E-04	0.59735	1.15424	0.34151	0.0192	7.29E-06
2.8	3.18157	0.39189	4.62E-04	0.57869	1.41772	0.33383	0.01248	1.98E-05
3	3.02299	0.58035	4.87E-04	0.5625	1.48702	0.30037	0.00902	5.39E-06
3.5	1.93509	0.95366	1.78E-04	0.39163	2.3657	0.33762	0.00355	1.02E-05
4	0	1.17818	1.00E+30	0	2.97192	0.39308	0.00102	1.25E-04
4.5	0	1.21369	1.00E+30	0	2.64471	0.35156	6.80E-04	7.28E-05
5	0	2.37284	1.00E+30	0	1.25113	1.68312	4.73E-04	1.48E-05
5.5	0	1.24945	1.00E+30	0	2.15956	0.3043	3.06E-04	7.19E-06
6	0	1.21656	1.00E+30	0	1.98387	0.32882	1.73E-04	1.35E-05

Table S10. Best fitted parameters (χ_T, χ_S, τ and α) with the extended Debye model for compound **[(*S*)-1]** at 1000 Oe in the temperature range 2-8 K.

T / K	$\chi_{T,1}$ / cm^3 mol^{-1}	χ_S / cm^3 mol^{-1}	τ_1 / s	α_1	$\chi_{t,2}$ / cm^3 mol^{-1}	α_2	τ_2 / s	R^2
2	4.0968	0.35598	3.98E-04	0.52695	1.53336	0.44287	0.06482	2.72E-05
2.2	3.87657	0.39091	3.61E-04	0.54691	1.43773	0.44529	0.0644	6.71E-05
2.4	3.43952	0.50278	2.92E-04	0.53899	1.61675	0.4708	0.05268	4.68E-05
2.6	3.48577	0.56512	3.55E-04	0.56528	1.25044	0.35024	0.05562	5.15E-05
2.8	3.23594	0.5871	2.98E-04	0.57521	1.27578	0.38874	0.04741	2.76E-05
3	3.03989	0.60427	2.49E-04	0.58304	1.23319	0.36715	0.03551	2.26E-05
3.5	2.50704	0.67641	1.35E-04	0.56922	1.36422	0.38995	0.01896	2.03E-05
4	0	1.54169	1.00E+30	0	2.82969	0.47155	4.19E-03	2.67E-05
4.5	0	1.45157	1.00E+30	0	2.51408	0.43529	2.85E-03	3.78E-05
5	0	1.42338	1.00E+30	0	2.2536	0.37403	2.39E-03	2.89E-05
5.5	0	1.25936	1.00E+30	0	2.06371	0.4071	1.22E-03	6.24E-05
6	0	1.20804	1.00E+30	0	1.89126	0.38648	8.92E-04	4.49E-05
7	0	1.17114	1.00E+30	0	1.61993	0.31695	6.39E-04	2.02E-05
8	0	1.12251	1.00E+30	0	1.4201	0.27963	4.52E-04	1.76E-05

Table S11. Calculated relative energies (ΔE, cm^{-1}), EPR g-factors and wavefunction compositions of the lowest Kramers doublet states for the solution **[(*S*)-1]** and solid-state **[(*S*)-1]$_n$** species.

	ΔE	g_x	g_y	g_z	$\|15/2, M_J\rangle$
Solution **[(*S*)-1]**					
GS	0	0.14	0.15	19.57	97 |±15/2>
ES1	103	0.50	6.98	10.24	28 |±9/2> + 20 |±13/2> + 20 |±7/2>
ES2	120	0.18	5.92	10.07	33 |±11/2> + 31 |±13/2> + 14 |±1/2>
ES3	131	4.74	7.08	9.39	41 |±13/2> + 31 |±11/2> + 8 |±7/2>
ES4	166	1.36	2.31	11.49	51 |±9/2> + 35 |±7/2> + 5 |±5/2>
ES5	185	0.34	1.99	9.62	32 |±5/2> + 29 |±11/2> + 21 |±7/2>
ES6	207	1.44	3.39	13.30	43 |±3/2> + 24 |±5/2> + 13 |±1/2>
ES7	601	0.00	0.00	19.82	43 |±1/2> + 31 |±3/2> + 16 |±5/2>
Solid-State **[(*S*)-1]$_n$**					
GS	0	0.02	0.14	19.70	98 |±15/2>
ES1	30	0.06	0.22	18.95	21 |±1/2> + 21 |±3/2> + 20 |±5/2>
ES2	76	0.83	0.97	16.53	25 |±9/2> + 23 |±7/2> + 16 |±5/2>
ES3	100	2.89	4.39	12.81	58 |±13/2> + 18 |±11/2> + 8 |±1/2>
ES4	113	2.73	4.30	12.51	31 |±11/2> + 21 |±13/2> + 18 |±9/2>
ES5	139	0.07	1.82	17.03	28 |±7/2> + 23 |±9/2> + 15 |±11/2>
ES6	154	0.10	1.64	15.24	27 |±5/2> + 20 |±3/2> + 19 |±11/2>
ES7	447	0.00	0.00	19.84	39 |±1/2> + 30 |±3/2> + 18 |±5/2>
Solid-State **[(*S*)-1]$_n$'**					
GS	0	0.03	0.15	19.64	98 |±15/2>

ES1	25	0.06	0.22	18.93	22 |±1/2> + 21 |±3/2> + 20 |±5/2>
ES2	71	1.11	1.33	16.06	27 |±9/2> + 22 |±7/2> + 15 |±5/2>
ES3	98	1.28	3.43	12.73	55 |±13/2> + 21 |±11/2> + 8 |±1/2>
ES4	112	3.85	5.74	11.15	28 |±11/2> + 24 |±13/2> + 20 |±9/2>
ES5	142	0.59	1.44	16.86	25 |±7/2> + 22 |±9/2> + 18 |±11/2>
ES6	156	0.14	1.57	15.70	28 |±5/2> + 23 |±3/2> + 14 |±11/2>
ES7	445	0.00	0.00	19.85	39 |±1/2> + 30 |±3/2> + 18 |±5/2>

Table S12. TD-DFT calculated absorption energies and main compositions of the low-lying electronic transitions for **(*S*)-L**. H and L represent the HOMO and LUMO, respectively. The theoretical values are evaluated at the PCM(CH_2Cl_2)-PBE0/SVP level of approximation.

Energy exp (cm^{-1})	Energy theo (cm^{-1})	Osc.	Transition
31000	32804	0.14	H→L (96%)
34500	35643 36360	0.05 0.06	H→L+2 (25%) H-1→L+1 (96%) H-4→L (27%)
38200	41387	0.06	H-1→L+4 (33%) H→L+2 (41%)
43000	45410 45725	0.70 0.35	H-1→L+6 (19%) H-8/-9→L+1 (41%)